# Scaling laws in gravitational clustering for counts-in-cells and mass functions

P. Valageas,[1,2,3] C. Lacey[2] and R. Schaeffer[1]

[1]*Service de Physique Théorique, CEA Saclay, 91191 Gif-sur-Yvette, France*
[2]*Theoretical Astrophysics Center, Juliane Maries Vej 30, 2100 Copenhagen O, Denmark*
[3]*Center for Particle Astrophysics, Department of Astronomy and Physics, University of California, Berkeley, CA 94720-7304, USA*

**ABSTRACT**

We present an analysis of some of the properties of the density field realized in numerical simulations for power-law initial power spectra in the case of a critical density universe. We study the non-linear regime, which is the most difficult to handle analytically, and we compare our numerical results with the predictions of a specific hierarchical clustering scaling model that have been made recently, focusing specifically on its much wider range of applicability, which is one of its main advantages over the standard Press–Schechter approximation. We first check that the two-point correlation functions, measured from both counts-in-cells and neighbour counts, agree with the known analytically exact scaling requirement (i.e., depend only on $\sigma^2$), and we also find the stable-clustering hypothesis to hold. Next, we show that the statistics of the counts-in-cells obey the scaling law predicted by the above scaling model.

Then we turn to mass functions of overdense and underdense regions, which we obtain numerically from 'spherical overdensity' and 'friends-of-friends' algorithms. We first consider the mass function of 'just-collapsed' objects defined by a density threshold $\Delta = 177$, and we note, as was found by previous studies, that the usual Press–Schechter prescription agrees reasonably well with the simulations (although there are some discrepancies). On the other hand, the numerical results are also consistent with the predictions of the scaling model. Next, we consider more general mass functions (needed to describe for instance galaxies or Lyman-$\alpha$ absorbers) defined by different density thresholds, which can even be negative. The scaling model is especially suited to account for such cases, which are out of reach of the Press–Schechter approach, and it still shows reasonably good agreement with the numerical results. Finally, we show that mass functions defined by a condition on the radius of the objects also satisfy the theoretical scaling predictions.

Thus we find that the scaling model provides a reasonable description of the density field in the highly non-linear regime, for the cosmologies we have considered, for both the counts-in-cells statistics and the mass functions. The advantages of this approach are that it clarifies the links between several statistical tools and it allows one to study many different classes of objects, for any density threshold, provided one is in the fully non-linear regime.

**Key words:** galaxies: clusters: general – cosmology: theory – large-scale structure of Universe.

## 1 INTRODUCTION

In the standard cosmological scenario large-scale structures in the Universe arise from the amplification through gravitational instability of small primordial density fluctuations. These initial perturbations are likely to be Gaussian (as in most inflationary models) and are characterized by their power spectrum. Within the hierarchical clustering scenario, the amplitude of these fluctuations increases towards the smaller scales (as in the CDM model: Peebles 1982; Davis et al. 1985). Small scales collapse first to form bound objects which merge later to build increasingly massive haloes as larger scales become non-linear. These mass condensations correspond to the various astrophysical objects one can observe in the Universe, from Lyman-$\alpha$ clouds to galaxies and clusters. As a consequence, to understand the formation of these objects it is important to obtain a precise description of the

evolution of the density field under the action of gravity. Note that to model specific astrophysical objects one usually needs to add to this description of dark matter haloes non-gravitational effects (such as, for instance, radiative processes to get the evolution of baryons). This is beyond the scope of the present paper that considers specifically the multiplicity of dark haloes.

However, even for the problem of the evolution of the matter distribution under the sole action of gravity theoretical results are very scarce. Linear theory allows one to describe the density field on large scales, while a few approximations (see, e.g., Bernardeau 1996) try to handle the early non-linear evolution, but the highly non-linear regime has proved very difficult to model. As a consequence, numerical simulations have so far been the main tool to describe this latter stage. In this paper we compare the results of simulations for power-law initial spectra in the case of a critical density universe with the scaling model presented in previous publications (Balian & Schaeffer 1989a; Bernardeau & Schaeffer 1991; Valageas & Schaeffer 1997, hereafter VS). This latter description of the density field is based on the assumption that the many-body correlation functions satisfy specific scaling laws (obtained from the stable-clustering Ansatz) in the highly non-linear regime. In this case one obtains a very powerful model for the density field, which can be used to obtain the counts-in-cells statistics as well as mass functions of overdense and underdense regions at different density thresholds. Note that in contrast the Press–Schechter (PS) mass function (Press & Schechter 1974), which is certainly the most popular tool to get some information on the characteristics of the non-linear density field, deals only with 'just-collapsed' objects.

The paper is organized as follows. In Section 2 we describe the numerical simulations we analyse. Then we present our results for the two-point correlation function and the counts-in-cells statistics in Section 3. We compare the numerical mass function of 'just-collapsed' objects to the usual PS prescription and to the scaling model in Section 4. We also consider more general mass functions, beyond the reach of the PS approach, that are defined by various density thresholds. Finally, we present our results for the limiting case of mass functions of objects defined by a constant radius constraint. These studies originate from astrophysical descriptions of galaxies (Valageas & Schaeffer 1999; Valageas & Silk 1999) and Lyman-$\alpha$ clouds (Valageas, Schaeffer & Silk 1999), where one is naturally led to introduce such generalized mass functions.

## 2 SIMULATIONS

We shall consider a critical density universe, $\Omega = 1$, with an initial power spectrum $P(k)$ which is a power law: $P(k) \propto k^n$. We study the cases $n = -2$, $n = -1$ and $n = 0$. As usual, we shall define $\sigma^2(R, a)$ to be the amplitude of the density fluctuations in cells of physical radius $R$ at time $t$ (scalefactor $a$) given by linear theory. Thus we have

$$\sigma^2 \propto a^2 r^{-(n+3)} \propto a^{(n+5)} R^{-(n+3)},\qquad(1)$$

where $r = R/a$ is a comoving scale.

The $N$-body simulations were performed using the $AP^3M$ code of Couchman (1991). The nominal box size was $L = 256\,h^{-1}$ Mpc (although this could be rescaled to any value, since the initial conditions are scale-free). The simulations all used $N_p = 128^3 \approx 2 \times 10^6$ particles, with a force-softening parameter (constant in comoving coordinates) of 0.1 times the mean interparticle

separation $L/N_p^{1/3}$, that is over a comoving radius of $0.2\,h^{-1}$ Mpc. The expansion factor $a$ was normalized so that $\sigma(R, a) = 1$ for $R = 8\,h^{-1}$ Mpc at $a = 1$, according to linear theory. The initial positions and velocities of the particles were given by displacing the particles from a cubical grid using the Zel'dovich approximation and the linear theory power spectrum. The starting time was chosen small enough so that the density fluctuations on the scale of the particle grid were still close to the linear regime. Specifically, the linear power spectrum amplitude at the Nyquist frequency of the particle grid was chosen to be $A^2$ times the white noise value, with $A = 1$ for $n = 0$ and $n = -1$, and $A = 0.4$ for $n = -2$, corresponding to expansion factors $a_i = 0.0611, 0.15$ and $0.194$ for $n = 0, -1$ and $-2$ respectively. For $n = 0$ the simulation was evolved with a constant time-step $\Delta p = 2.36 \times 10^{-3}$ in the variable $p = a^{2/3}$, while for $n = -1$ and $-2$ a constant timestep in $a$ was used, with $\Delta a = 3.4 \times 10^{-3}$ and $1.5 \times 10^{-3}$ respectively. The simulations were evolved up to expansion factors $a_f = 8, 4$ and $2.67$ for $n = 0, -1$ and $-2$ respectively. In the numerical analysis we shall use the output times in the range $1 \leq a \leq a_f$ when some non-linear structures have already formed on scales larger than the smoothening length.

For this cosmology and initial power spectra, the real clustering evolution should be *self-similar*, when scaled to a radius $R_*(a) \propto a^{(n+5)/(n+3)}$ such that $\sigma(R_*, a) = 1$. This is an exact analytical result that holds independently of the validity of the Balian & Schaeffer (1989a) *scaling* predictions (see Section 3) that we aim at testing in this paper. The evolution in the $N$-body simulation will depart from exact self-similarity because of numerical effects, in particular, particle discreteness, force softening, the finite box size, and the absence of initial fluctuations smaller than the Nyquist wavelength or larger than the box size.

## 3 COUNTS-IN-CELLS

A convenient way to describe the density field obtained in a numerical simulation, or realized in the actual Universe, is to consider the counts-in-cells. Thus we define the probability distribution $P_R(N; t)$ to be the probability to have $N$ particles in a spherical cell of radius $R$ at a given time $t$. In the following we shall usually denote $P_R(N; t)$ as $P(N)$ to simplify the notation. This is a well-defined quantity which provides a very good description of the density field and is a convenient tool for a theoretical analysis. In contrast, the multiplicity functions used to recover the counts of virialized haloes or astrophysical objects may be defined in various ways and are somewhat more difficult to handle analytically. However, in certain regimes their properties can be obtained from the characteristics of the counts-in-cells. Hence we shall first consider the statistics of $P(N)$ in the next sections.

### 3.1 Non-linear scaling model

Since we shall mainly compare our results with the scaling model described in Balian & Schaeffer (1989a), we recall here their predictions while introducing our notation. This model is based on the assumption that the many-body correlation functions $\xi_p(\boldsymbol{r}_1, ..., \boldsymbol{r}_p; a)$ satisfy the scaling law:

$$\xi_p(\lambda\boldsymbol{r}_1, ..., \lambda\boldsymbol{r}_p; a) = a^{3(p-1)}\lambda^{-\gamma(p-1)}\hat{\xi}_p(\boldsymbol{r}_1, ..., \boldsymbol{r}_p),\qquad(2)$$

where $a(t)$ is the scalefactor, and $\gamma$ is the slope of the two-point correlation function (which we note $\xi$). For an initial power

spectrum $P(k)$ which is a power-law, $P(k) \propto k^n$, we have

$$\gamma = \frac{3(3+n)}{5+n}. \tag{3}$$

The relations (2) and (3) are derived from the stable-clustering assumption (Davis & Peebles 1977; Peebles 1980) and are expected to describe the highly non-linear regime $\bar{\xi} \gg 1$. To obtain the statistics of $P(N)$ in cells of radius $R$, volume $V$, it is convenient to define the quantities

$$S_p = \frac{\bar{\xi}_p}{\bar{\xi}^{p-1}} \quad \text{with} \quad \bar{\xi}_p = \int_V \frac{d^3r_1 \ldots d^3r_p}{V^p} \xi_p(r_1, \ldots, r_p). \tag{4}$$

Then,

$$P(N) = \frac{1}{N_c \bar{\xi}} h(x) \quad \text{with} \quad x = \frac{N}{N_c} = \frac{1+\Delta}{\bar{\xi}} \tag{5}$$

in the regime where

$$N \gg N_v \quad \text{and} \quad N_c \gg N_v. \tag{6}$$

Here we defined

$$N_c = \bar{N}\bar{\xi}, \quad N_v = \frac{\bar{N}}{\bar{\xi}^{\omega/(1-\omega)}}, \quad \bar{N} = \bar{n}V, \quad 1+\Delta = \frac{N}{\bar{N}}, \tag{7}$$

where $\bar{n}$ is the average number density in the simulation. It is also required that the continuous limit $N \gg 1$ is reached in the relevant sampling of the simulation. The two conditions (6) ensure that (i) the counts are relevant to mass condensations and not to 'voids', and (ii) one is in the fully non-linear regime where $\bar{\xi}$ is large so that the non-linear scaling represented by $h(x)$ can develop. The scaling (5) implies that

$$p \geq 1 : S_p = \int_0^\infty x^p h(x)\, dx, \quad S_1 = S_2 = 1. \tag{8}$$

From very general considerations one expects that

$$\begin{cases} x \ll 1 : \quad h(x) \sim \dfrac{a(1-\omega)}{\Gamma(\omega)} x^{\omega-2} \\ x \gg 1 : \quad h(x) \sim a_s x^{\omega_s-1}\, e^{-x/x_s}, \end{cases} \tag{9}$$

where $x_s$ is a constant, typically of order 10. Thus $P(N)$ shows a power-law behaviour in the range $N_v \ll N \ll N_c$ and an exponential cut-off for $N \gg N_c$.

If the scaling laws (2) apply, then the ratios $S_p$ and the function $h(x)$ are independent of scale and time. This means that once $h(x)$ is given (e.g., from measures performed at a certain scale and time), one only needs to know the evolution of the two-point correlation function $\bar{\xi}$ to be able to construct the whole statistics of $P(N)$ at any scale and time in the highly non-linear regime. Since $\bar{\xi}$ obeys (2), its evolution is known in the non-linear regime once its normalization is measured for one scale and time.

### 3.2  The two-point correlation function

#### 3.2.1  Fluctuations in a cell

As we described in the previous section, in order to test the scaling model in the domain $N \gg N_v$ we first need the evolution of the two-point correlation function $\bar{\xi}$. Moreover, $\bar{\xi}$ presents a strong interest in itself since it gives a measure of the amplitude of the density fluctuations and it provides a first check of the stable-clustering assumption. Indeed, if the latter holds the slope $\gamma$ of $\bar{\xi}(R)$ must be given by (3).

To get $\bar{\xi}(R)$ we simply count the number of particles enclosed in each of $300^3$ spheres of radius $R$ set on a grid and we measure $\langle N \rangle$ and $\langle N^2 \rangle$, where $\langle \rangle$ denotes an average over all trials. Then we use the relation

$$\bar{\xi} = \frac{\langle N^2 \rangle}{\langle N \rangle^2} - 1 - \frac{1}{\langle N \rangle} \tag{10}$$

As argued by VS, following the ideas of Hamilton et al. (1991) from a Lagrangian point of view where one follows the evolution of matter elements, one expects $\bar{\xi}(R, a)$ to be closely related to the linear correlation function $\sigma^2(R_L, a)$ evaluated at a different scale $R_L$ but at the same time:

$$\begin{cases} \bar{\xi}(R, a) = F[\sigma^2(R_L, a)] \\ R_L^3 = [1 + \bar{\xi}(R, a)]R^3. \end{cases} \tag{11}$$

In fact, since our initial conditions are scale-invariant, the relation (11) is *exact*: it is then just a rewriting of the scaling solution of Peebles (1980) that holds in this case. Its main interest comes from its physical interpretation which suggests that the $F(\sigma^2)$ obtained for various $n$ should show a similar behaviour. Of course, in the linear regime $\bar{\xi} \ll 1$ we must recover $\bar{\xi} \simeq \sigma^2$, while in the highly non-linear regime, if clustering is stable, we have $\bar{\xi}(R, a) \propto a^3$. This gives the asymptotic behaviour of the function $F(\sigma^2)$:

$$\begin{cases} \sigma \ll 1 : \quad F(\sigma^2) = \sigma^2 \\ \sigma \gg 1 : \quad F(\sigma^2) = \left(\dfrac{10}{3\alpha}\right)^3 \sigma^3, \end{cases} \tag{12}$$

where $\alpha \simeq 1$. As a consequence, we plot the values of $\bar{\xi}(R)$ obtained from the simulations through (10) as a function of $\sigma^2(R_L)$ rather than $R$. Thus, at a given scale $R$ we measure $\bar{\xi}(R)$, and we know $\sigma^2(R)$ from which we derive $\sigma^2(R_L) = \sigma^2(R)\, (R_L/R)^{-(n+3)} = \sigma^2(R)\, (1+\bar{\xi})^{-(n+3)/3}$. The results are shown in Fig. 1 for various $n$.

Since the initial conditions of the simulation are scale-invariant [$P(k)$ is a power law] all curves should superpose as long as numerical effects (finite box size, softening length and resolution scale) are small. We can check that this is indeed the case. Moreover, in the highly non-linear regime we recover the asymptotic behaviour given by (12), which is shown by the solid line. The normalization parameter $\alpha$ is displayed in Table 1 for the three power spectra. However, we can note that for larger scales the two-point correlation function 'saturates' to a value lower than its asymptotic limit. This problem increases for smaller $n$, and is due to numerical effects since, as we explained above, all curves should superpose. The dependence on scale and on $n$ of this effect shows that it is produced by the lack of power in the simulation at large scales. Indeed, the actual initial power spectrum $P(k)$ is a power law only over a limited range of $k$, and the influence of the numerical cut-off at $k_{min}$, unduely supressing some power, becomes more important as one considers larger scales (hence wavenumbers closer to $k_{min} = 2\pi/L$) and lower $n$ (which increases the contribution of small $k$). Similarly, there is a high frequency cut-off. The correlation function $\xi$ starts to deviate from the exact scaling imposed by our power-law initial conditions when the sampling of the numerical output is done at the 0.2 Mpc comoving scale and below. This is very distinctly seen in Fig. 1 for the larger values of the correlation function. This is due to the softening of the interaction, which for all the samples we use is done over a radius of 0.2 Mpc (comoving). Again, the

result is a lack of power, due to this softening. Obviously, the deficit is larger for $n = 0$ than for $n = -2$, the former case, with more small-scale power, being more sensitive to this effect.

Note that the Nyquist frequency and particle discreteness play a
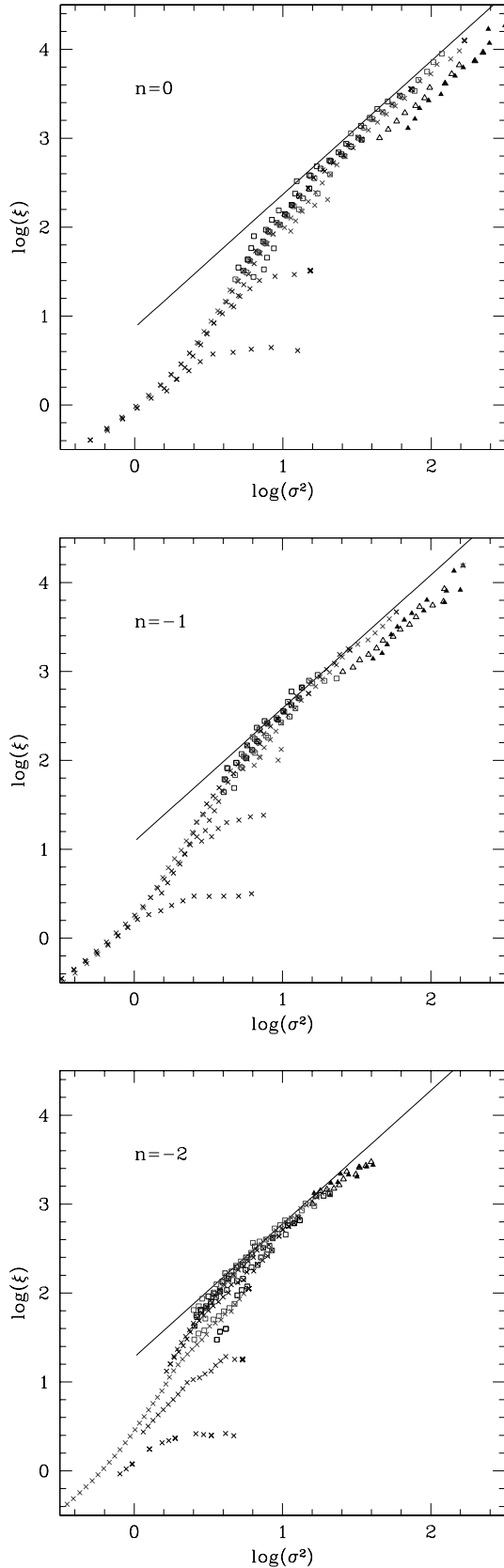


**Table 1.** Normalization parameters for the two-point correlation functions. The non-linear exponent $\gamma$ is given by equation (3). The columns (J) and (C) correspond to the numerical results obtained by Jain et al. (1995) and Colombi et al. (1996); see text. Note that the ratio $\alpha/\bar{\alpha}$ is predicted by the stable-clustering Ansatz; see equation (16).

| $n$ | $\gamma$ | $\alpha/\bar{\alpha}$ | $\alpha$ | $\alpha$ (J) | $\alpha$ (C) | $\bar{\alpha}$ | $\bar{\alpha}$ (J) | $\bar{\alpha}$ (C) |
|---|---|---|---|---|---|---|---|---|
| 0 | 1.8 | 1.10 | 1.71 | 1.43 | 1.28 | 1.55 | 1.30 | 1.16 |
| $-1$ | 1.5 | 0.95 | 1.45 | 1.18 | 1.33 | 1.52 | 1.24 | 1.40 |
| $-2$ | 1 | 0.96 | 1.25 | 1.09 | 1.25 | 1.30 | 1.13 | 1.30 |

minor role if any at all, since we consider only the cases where the number of points in the simulation is large enough.

### 3.2.2 Counts of neighbours

Although the average $\bar{\xi}$ defined by (4) appears naturally when one considers counts-in-cells, many authors studied the quantity $\tilde{\xi}$ given by

$$\tilde{\xi}(R) = \frac{3}{R^3} \int_0^R \xi(r) r^2 \, \mathrm{d}r, \tag{13}$$

which is relevant for the counts of neighbours. Indeed, the mean number of neighbours located within a radius $R$ from a given particle is

$$\langle N_{\mathrm{nb}} \rangle = \langle N \rangle [1 + \tilde{\xi}(R)]. \tag{14}$$

For a power-law power spectrum, $\tilde{\xi}$ depends on its linear equivalent $\tilde{\sigma}^2$ in a fashion similar to (11), with a new function $\tilde{F}$, which has the same asymptotic behaviour as (12), but with a slightly different normalization $\tilde{\alpha}$ (Peebles 1980; Hamilton et al. 1991; see also Padmanabhan 1996). We measure $\tilde{\xi}$ in the simulation using (14): we count the mean number of neighbours of particles in the box which gives $\langle N_{\mathrm{nb}} \rangle$, while the total number of points in the simulation provides $\langle N \rangle$. The result is shown in Fig. 2. We indeed recover the behaviour predicted by (12). This confirms the previous results of Fig. 1, since both $\bar{\xi}$ and $\tilde{\xi}$ are measures of $\xi$. This shows that in the non-linear regime the stable-clustering Ansatz holds for $\xi$, which obeys the scaling law (2).

Moreover, the measure of $\tilde{\xi}$ allows us to get a second estimate of $\bar{\xi}$ in the non-linear regime. Indeed, in the domain where $\bar{\xi} \gg 1$ the two-point correlation function is a power-law with a slope $\gamma$ given by (3) as shown by Figs 1 and 2. In this case, one can show (Peebles 1980) that

$$\tilde{\xi}(R) = \beta \bar{\xi}(R) \quad \text{with} \quad \beta = (1 - \gamma/4)(1 - \gamma/6)2^\gamma. \tag{15}$$

**Figure 1.** The two-point correlation function $\bar{\xi}(R)$ as a function of $\sigma^2(R_{\mathrm{L}})$ for the power spectra $n = 0, -1$ and $-2$. The solid line is the asymptotic behaviour (12) for large $\bar{\xi}$, in the stable-clustering regime, with normalization $\alpha$ from Table 1. The crosses are numerical values obtained from counts-in-cells, while the squares are the estimates of $\bar{\xi}$ provided by measures of $\tilde{\xi}$ from neighbour counts; see main text and (15). Different shades of grey correspond to different comoving scales (0.2, 0.5, 1, 2, 4, 8 and 16 Mpc). The filled (respectively open) triangles show the results for 0.2 Mpc from counts-in-cells (respectively neighbour counts). The larger scales (8 and 16 Mpc) saturate at too low a value of $\bar{\xi}$, reflecting the finite size of the sample. The 0.2-Mpc scale presents deviations from the scaling in the highly non-linear regime (all curves should exactly superpose for our power-law initial conditions), with a lack of power due to the softening – over a 0.2-Mpc radius – of the gravitational interaction.
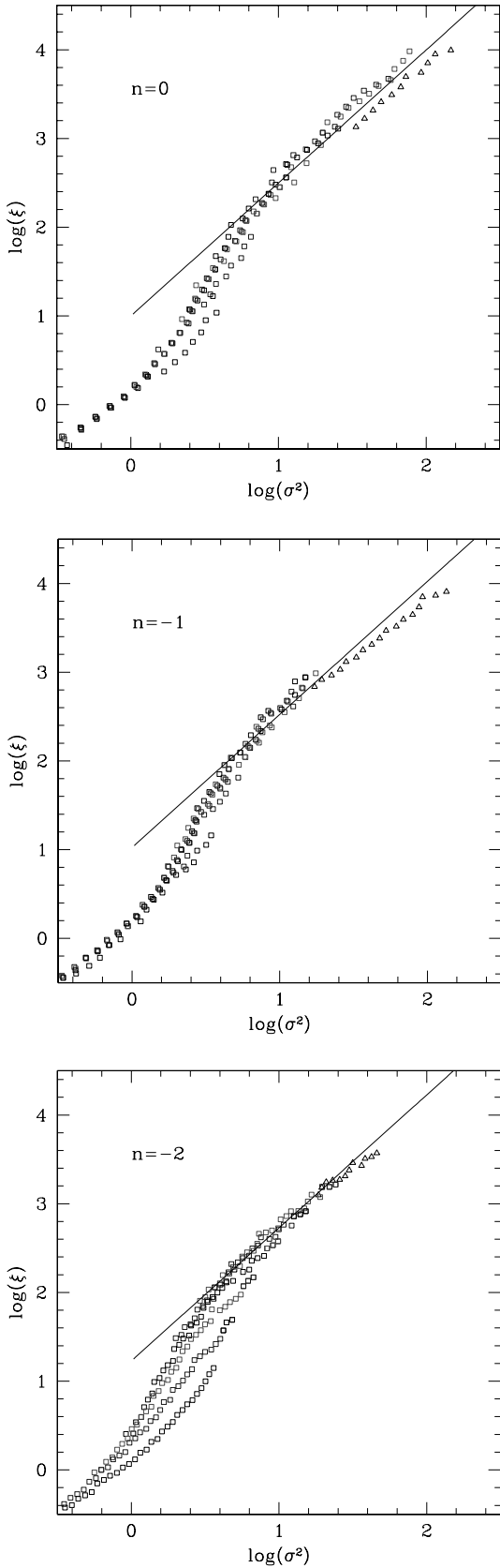
**Figure 2.** The two-point correlation function $\tilde{\bar{\xi}}(R)$ (obtained from neighbour counts) as a function of $\bar{\sigma}^2(R_L)$ for the power spectra $n = 0, -1$ and $-2$. The solid line is the asymptotic behaviour (12) for large $\bar{\xi}$, with the normalization parameter $\tilde{\alpha}$ from Table 1. The triangles correspond to the comoving scale 0.2 Mpc. See Fig. 1 and the text for comments.

Thus we can obtain $\bar{\xi}(R)$ from the measure of $\tilde{\bar{\xi}}(R)$. These values are shown by squares in Fig. 1. We can check that they agree with the previous calculations for $\bar{\xi}$ based on the counts-in-cells. Note that we only show in Fig. 1 the values of $\bar{\xi}$ obtained from $\tilde{\bar{\xi}}$, through (15), which are in the highly non-linear regime $\bar{\xi} \gg 1$ where the two-point correlation function is a power law so that (15) applies. Note that in this case (compare Fig. 1 with Fig. 2), the lack of power at the larger scales is much less pronounced: the count of neighbours already focuses on the dense regions and the statistics of the poorly represented events at large scale is improved. Indeed, to measure $\tilde{\bar{\xi}}$ one considers cells which are centred on particles (hence this statistical tool follows the evolution of gravitational clustering as it automatically probes more closely denser regions), while to get $\bar{\xi}$ the centre of the cells is set at random in the box, so that in the highly non-linear regime most cells are within voids. Thus at least part of the deviations seen at these scales are due to the statistical extraction of the information.

We present in Table 1 the values of the normalization parameters $\alpha$ and $\tilde{\alpha}$ obtained from our simulation, as well as from Jain, Mo & White (1995) and Colombi, Bouchet & Hernquist (1996). For the former we calculate $\alpha$ from their value of $\tilde{\alpha}$, while for the latter we obtain $\tilde{\alpha}$ from $\alpha$. Indeed, from (15) we get

$$\alpha = \tilde{\alpha} \beta^{1/3} \beta_L^{-1/2}, \tag{16}$$

where $\beta$ (respectively $\beta_L$) is given by (15) with $\gamma = 3(3 + n)/(5 + n)$ [respectively $\gamma = (3 + n)$], corresponding to the non-linear (respectively linear) regime. Although all numerical simulations agree with the stable-clustering Ansatz: (3), (11) and (12), the normalization of $\bar{\xi}$ in the non-linear regime varies up to a factor of 2 (note that it scales as the cube of $\alpha$). Thus there is still some inaccuracy in the numerical values of $\bar{\xi}$. Moreover, one may expect the higher order correlation functions (hence the parameters $S_p$) to bear at least similar uncertainties. The discrepancies between the various estimates of $\alpha$ may be due to the effects of finite volume and particle number: in particular, the initial power spectrum is not a power-law over an infinite range of scales (there are an upper and a lower cut-off) and one should average $\bar{\xi}$ over many realizations of the initial Gaussian field. However, the fact that curves obtained from different scales superpose in Figs 1 and 2 and that our measures of $\tilde{\bar{\xi}}$ are consistent with $\bar{\xi}$ shows that we can reasonably rely on our results. Except in the extreme cases where the finiteness of the sample (at large scales) or the smoothing of the force (at small scales) become important, *these results are consistent with the idea that the stable-clustering regime is reached* (see, however, Padmanabhan et al. 1996 for an alternative view).

### 3.2.3 Analytical fit to the fluctuations in a cell

We show in Fig. 3 the relation $\sigma^2(R) \leftrightarrow \bar{\xi}(R)$. This corresponds to an Eulerian point of view as opposed to the Lagrangian point of view displayed in Fig. 1, since we now consider the values of the linear and non-linear correlation functions taken at the same spatial scale (and not at the same 'mass scale'). We can note that the curves we obtain are quite smooth when displayed in this diagram, and they do not show a sharp 'step-profile' as was the case in Figs 1 and 2. The solid lines are analytical fits to the numerical results which we shall need below (Section 4) to get the mass functions within the framework of the scaling approach.
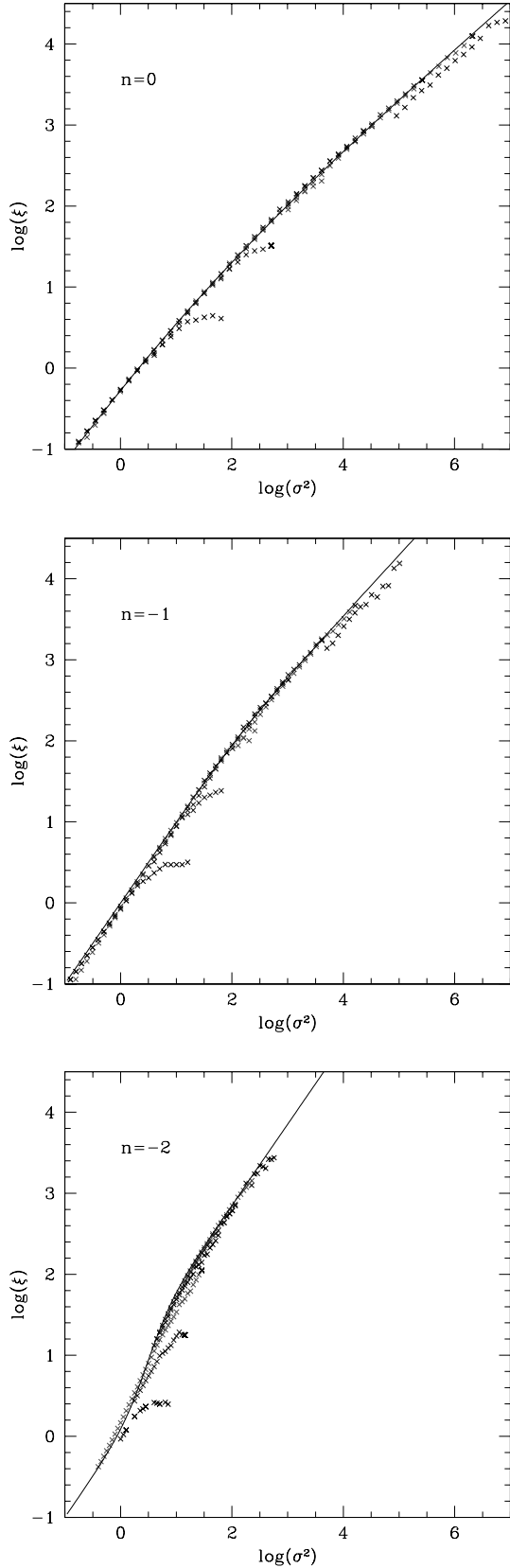
**Figure 3.** The two-point correlation function $\bar{\xi}(R)$ as a function of $\sigma^2(R)$ (hence taken at the same spatial scale). The crosses are numerical estimates from counts-in-cells in the simulations, while the solid lines are the analytical fits (17). See Fig. 1 and text for comments.

Thus we use the approximations:

$$\begin{cases} n = 0, 1 : \quad \bar{\xi}(R) \simeq [(\sigma^2)^{-a} + (\bar{\xi}_1)^{-a}]^{-1/a} \\ \quad \text{with } n = 0 : \quad a = 0.7; \quad n = -1 : \quad a = 4 \\ n = -2 : \quad \bar{\xi}(R) \simeq [\sigma^2 + (\sigma^2/5)^2 \bar{\xi}_1]/[1 + (\sigma^2/5)^2], \end{cases} \quad (17)$$

where $\bar{\xi}_1(R) = \left[\frac{10}{3\alpha}\sigma(R)\right]^{6/(5+n)}$. Of course, these fits are built so as to be consistent with (11) and (12). These relations define implicitly the functions $F(\sigma^2)$. They will be used instead of the correlation function $\bar{\xi}$ actually measured in the simulation (hence they will not be a source of unwanted deviations from self-similarity) when we determine the scaling properties of the multiplicity functions (Section 4).

### 3.3 Counts-in-cells statistics

By counting the number of particles enclosed in each of $300^3$ spheres set on a grid, as we did to evaluate $\bar{\xi}$, we can also obtain the statistics of the counts-in-cells. This allows us to compare the predictions (5) of the scaling model to our numerical results for $P(N)$. Note that we obtain simultaneously the value of $\bar{\xi}$ in the simulation, at the scale of interest, which we use in (5). We display the results in Fig. 4 as a function of $x$: from $N$ and $P(N)$ obtained by these counts in the simulation we define

$$x = \frac{N}{N_c} \quad \text{and} \quad x^2 h(x) = \frac{N^2}{\bar{N}} P(N). \quad (18)$$

If the scaling laws (2) hold, the quantity $h(x)$ used above must be the scaling function defined in (5). Then, all curves obtained for different sizes and times should superpose. Note that in our case where the initial power spectrum is a power law, all curves characterized by the same $\bar{\xi}$ (or equivalently by the same $\sigma^2$) must coincide. Thus the scaling laws (2) merely imply in addition that curves measured for different $\bar{\xi}$ should also superpose, when shown in a diagram $x \leftrightarrow x^2 h(x)$ as defined by (18).

We can see in Fig. 4 that the various curves indeed superpose, for all three power spectra. Note that in this figure we show only the parts of $P(N)$ which should scale as predicted by (5): we display only points which satisfy the requirements $\bar{\xi} > 100$, $N > 4$, $N > 4N_v$ and $N_c > 4$. The solid curves are analytical fits to the data points. We use the functional form introduced by Bouchet, Schaeffer & Davis (1991):

$$h(x) = \frac{a(1 - \omega)}{\Gamma(\omega)} \frac{x^{\omega - 2}}{(1 + bx)^c} \exp(-x/x_s). \quad (19)$$

The values of the parameters $a$, $\omega$, $b$, $c$ and $x_s$ are given in Table 2. Note that the functions $h(x)$ must also obey the constraints

$$\int_0^\infty x h(x)\, dx = \int_0^\infty x^2 h(x)\, dx = 1 \quad (20)$$

from the general relation (8).

The dashed curve in the figures is the function $h(x)$ which one obtains (see VS) by assuming that the non-linear evolution of initial density fluctuations is given by the PS approximation in the case where the correlation function has reached the stable clustering regime (which is indeed the case in the examples we have considered in Fig. 4). Thus we obtain what we shall refer to as the 'PSs' estimate ('s' for stable)

$$h_{\text{PSs}}(x) = \sqrt{\frac{2}{\pi}} \frac{5 + n}{6\alpha} x^{(n+5)/6 - 2} \exp\left[-\frac{x^{(5+n)/3}}{2\alpha^2}\right], \quad (21)$$

the result being multiplied by the standard 'PS factor' of 2. For the stable-clustering regime, $x < (1 + \Delta)/200$, this expression is identical to the usual PS formula (normally used for $\Delta \sim 177$, the usual density contrast of just-virialized haloes). If the above

**Table 2.** Parameters for the scaling function $h(x)$.

| $n$ | $a$ | $\omega$ | $x_s$ | $b$ | $c$ |
|---|---|---|---|---|---|
| 0 | 1.50 | 0.45 | 4 | 1 | 0.6 |
| $-1$ | 1.48 | 0.4 | 8 | 3 | 0.6 |
| $-2$ | 1.71 | 0.3 | 13 | 5 | 0.6 |
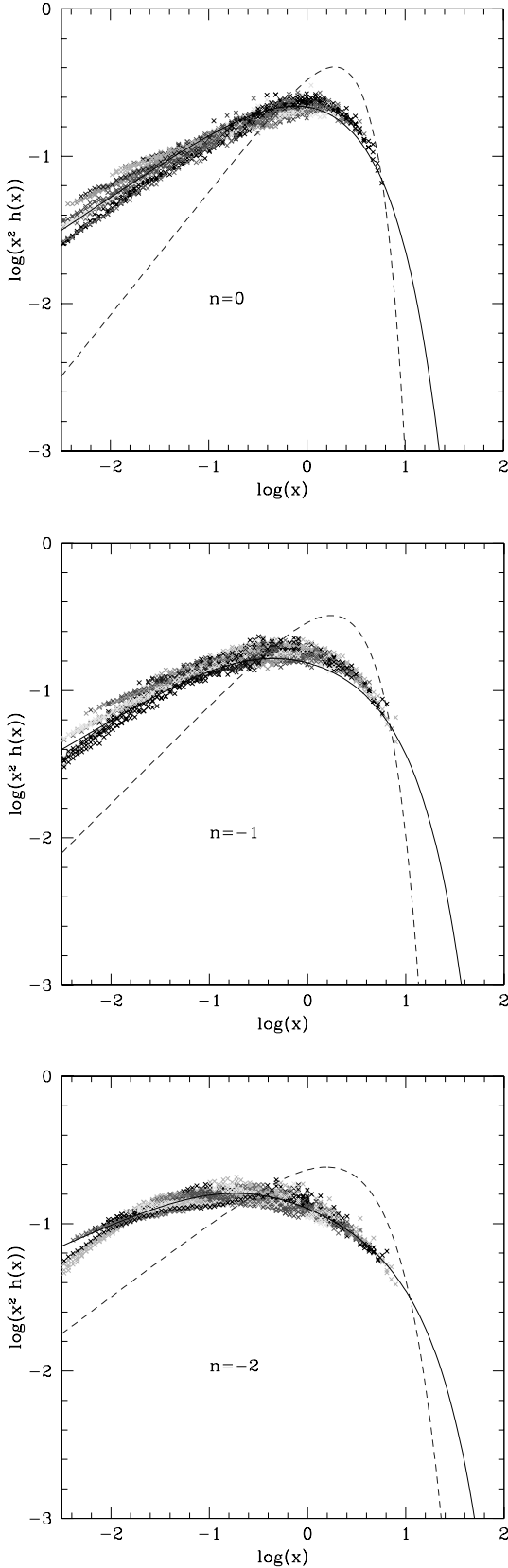
condition on $x$ is not fulfilled, only minor differences between the two expressions appear however; see Fig. 7 below. We can see in Fig. 4 that the function $h_{PSs}(x)$ obtained in this way does not agree with the numerical results, the true distribution being much broader as argued by VS (the general trend, however, larger $\omega$ and sharper cut-off for higher $n$, is correct). This means either that one cannot follow the evolution of individual matter elements with using only the spherical model, because there is some exchange of matter between neighbouring density fluctuations through mergers and disruptions, and the corrections to the spherical dynamics are not negligible, or that after virialization the density fluctuations still undergo non-negligible evolution. The stable-clustering Ansatz, on the other hand, is seen from Figs 1 and 4 to be a valid approximation in a statistical sense.

The scaling of the count-in-cells has thus been checked over an unprecedented range (more than 3 decades in the scaling parameter $x$). Note that we check here not only the scaling of the counts as a function of the cell size $R$ but also as a function of time, that is the self-similarity – in principle exact – of the computation results.

Although all curves at different scales superpose, building indeed the predicted universal $h(x)$ curve, some deviations are seen for small values of the parameter $x$. Clearly, these small values of $x$ [$\log(x) = -2.5$!], never reached in earlier simulations, are at the limit of the possibilities of the present calculations, but the deviations appear to be systematic. For larger $\bar{\xi}$ the function $h(x)$ appears to be slightly flatter, although it still obeys the constraints (20). Whether this effect is the sign of a real deviation of $h(x)$ from the predicted scaling, or is due to some bias in the simulation, warrants investigation. To this purpose, we can consider the same simulation results in more detail. In the continuous limit ($N \gg 1$), the expression $N^2/\bar{N} P(N)$, which in general depends on the three variables $N$, the cell size $R$ and the expansion parameter $a$, can always be written as $N^2/\bar{N}P(N) = x^2h(x, \bar{\xi}, R)$, the latter expression representing a simple change of the original variables into $x$, $\bar{\xi}$ and $R$. The exact self-similarity due to our power-law initial conditions implies that $N^2/\bar{N} P(N)$, as well as $\bar{\xi}$, are a function of the ratio $R/a^{(n+5)/(n+3)}$ only (i.e., they depend only on $\sigma$), and thus that $N^2/\bar{N}P(N) = x^2h(x, \bar{\xi})$ is independent of $R$, since $\bar{\xi}$ carries all the dependence on $R$ and $a$. The scaling prediction (due to the stable-clustering model) in addition states



**Figure 4.** The probability distribution $P(N)$ for counts-in-cells. We display the quantity $N^2/\bar{N}P(N) = x^2h(x)$ as a function of $x = N/N_c$. The solid curves are the analytical fits given by (19) and Table 2, while the dashed lines show the 'PSs' scaling function (21) obtained using the Press–Schechter approach in the regime where the correlation function has reached stable clustering. Different shades of grey correspond to different values of $\bar{\xi}$, ranging from 100 up to the highest value shown in Fig. 1. Only the scales (from 0.5 to 4 Mpc) where the correlation function is seen (Figs 1, 2 and 3) to obey the scaling required by the exact self-similarity are considered here and in the following.
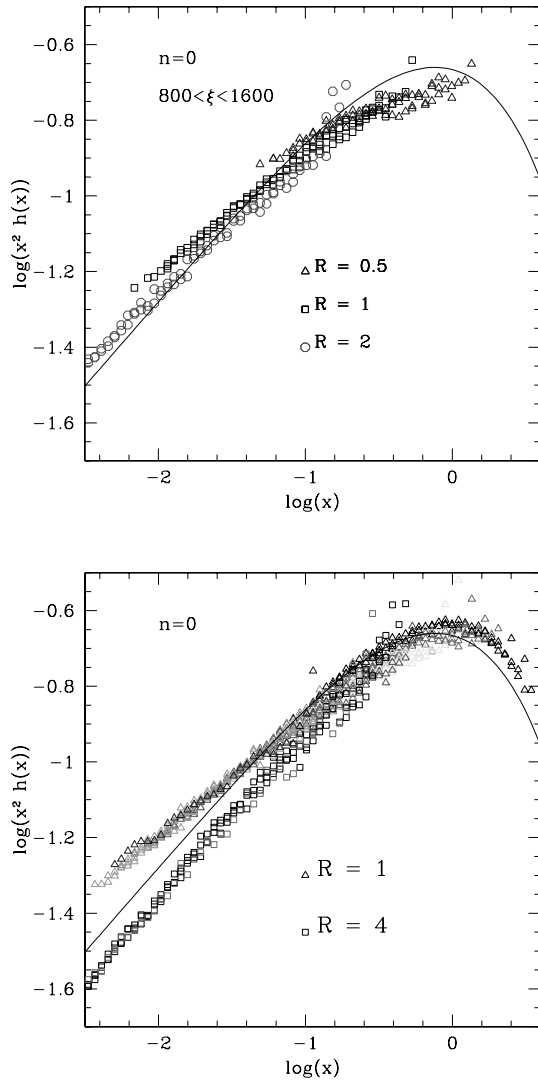
**Figure 5.** *Upper panel*: the probability distribution $P(N)$ for counts-in-cells as in Fig. 4 for $n = 0$ with the constraint $800 < \bar{\xi} < 1600$. We show the curves obtained for the three comoving scales $R = 0.5$ Mpc (triangles), $R = 1$ Mpc (squares) and $R = 2$ Mpc (circles). The solid curve is the analytical fit given by (19) and Table 2, as in Fig. 4. *Lower panel*: the curves for $P(N)$ obtained at fixed comoving $R$ by letting $\bar{\xi}$ (i.e., time) vary. We show the cases $R = 1$ Mpc (triangles) and $R = 4$ Mpc (squares). Different shades of grey correspond to different values of $\bar{\xi}$.

that in the limit of large $\bar{\xi}$, when the stable clustering regime is reached, $N^2/\bar{N} \, P(N)$ has a limit for fixed $x$ that is independent of $\bar{\xi}$. By definition of $h(x)$, this limit is $N^2/\bar{N}P(N) = x^2h(x)$. The scatter seen in Fig. 4 must have its origin in the violation of one of the two above conditions that are needed to get the seeked scaling function. As a first check, we can consider the variations with $R$ at fixed $\bar{\xi}$. The value of the latter ranging from 100 to 6400, typical intermediate values are $800 \leq \bar{\xi} \leq 1600$. In this range, values of $R = 0.5, 1$ and 2 Mpc are available. We can see in Fig. 5 (upper panel) that for these given values of $\bar{\xi}$, although the curves look reasonably close, there is a distinct drift at small $x$, the curves for the smaller values of $R$ lying systematically above the ones for the lower values. Also, the deviations get larger the smaller the value of $x$. Since we let $R$ vary for a fixed $\bar{\xi}$, this effect represents deviations from the 'exact' self-similarity
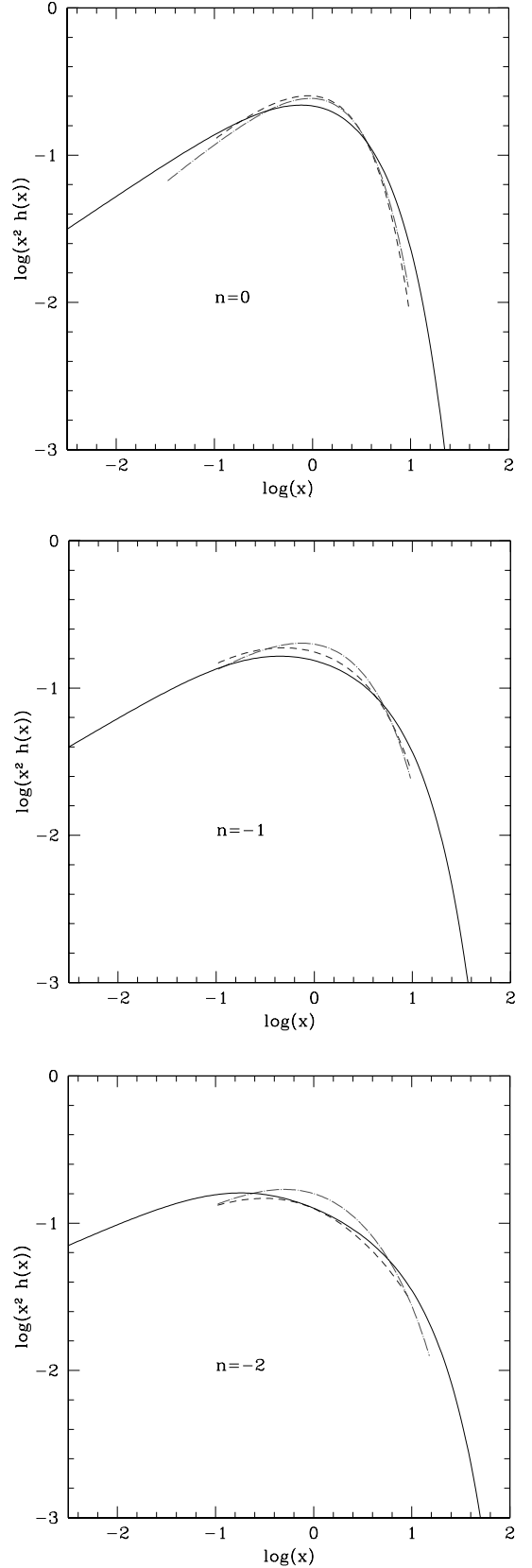
**Figure 6.** Comparison of the scaling function $x^2h(x)$ obtained from our simulations with the estimates given by Colombi et al. (1997) (dashed line) and Munshi et al. (1999) (dot-dashed line). For the latter two cases we display $x^2h(x)$ only in the range where it was actually tested against numerical data.

(implied by scale-invariant initial conditions) due to the unavoidable errors in the simulation. To estimate the size of these deviations, we show in Fig. 5 (lower panel) the probability distribution obtained for all possible values of $\bar{\xi}$ keeping $R$ fixed at two values (1 and 4 Mpc). For a given $R$, when $\bar{\xi}$ is varied, all curves superpose. However, when $R$ is changed, we get a different curve. This shows again that $N^2/\bar{N}$ $P(N)$ depends on $R$ and not on $\bar{\xi}$, with a deviation that reaches a factor of 2 at small $x$ ($x < 3 \times 10^{-3}$), of the order of magnitude of the scatter seen in Fig. 4. So we can attribute the observed scatter to deviations from the 'exact' self-similarity (due to a power-law initial power spectrum), hence to numerical inaccuracies and not to a violation of the non-linear scaling prediction that we aim to test here.

We compare in Fig. 6 the scaling functions $h(x)$ we get in our simulations with the results obtained by Colombi et al. (1997) and Munshi et al. (1999). For these two latter cases we display $h(x)$ only over the ranges where there were actually data points from the simulations (for our scaling function the range tested against numerical results can be directly seen from Fig. 4). We can check in the figure that all of the scaling functions agree fairly well with each other (within the numerical uncertainties which can be estimated from the dispersion shown in Fig. 4). Thus, although there is still some dispersion between the various estimates of $h(x)$, which could be expected from the discrepancies which already appeared for $\bar{\xi}$, the scaling function $h(x)$ is rather well constrained in the range where it has actually been tested, to an accuracy which is certainly sufficient for practical purposes. However, it should be noted that the range in $x$ available to constrain $h(x)$ is still too small to determine accurately the parameters of the fit (19) for low $n$, especially $x_s$ (there is some degeneracy between the exponential cut-off and the exponent $\omega_s$ of the power-law pre-factor). Thus, in the case $n = -2$, the values of $x_s$ obtained by Colombi et al. (1997) and Munshi et al. (1999) differ by a factor of 2, although both scaling functions are rather close over the range shown in Fig. 6. This means that the asymptotic behaviour of $h(x)$, and more generally its behaviour for $x \gtrsim 10$, typically is still rather poorly determined.

### 3.4    Moments of the counts-in-cells

If one believes that the scaling function $h(x)$ provides a reasonably good description of the counts-in-cells, it is readily seen from Fig. 4 that the measured counts in the simulation miss the very rare overdensities at $x \gtrsim 10$. In this region, actually there are counts that oscillate, due to (Bouchet et al. 1992; Colombi, Bouchet & Schaeffer 1995) whatever last cluster appears to be in the numerical data, reflecting their 'cosmic variance'. It turns out that the calculation of the moments $S_p$ (see equation 4) badly reflects this missing information. The moments directly obtained from the measured counts are systematically underestimated, the effect being more pronounced as the scale of the cells increases. The moments depend most on the counts-in-cells at $x \simeq (p + \omega_s)x_s$, as can be seen from (8) and (9). With $\omega_s \simeq -1$ and $x_s \simeq 10$ the calculation of $S_3$, already, cannot be done without an extrapolation of the numerical data to the badly needed, but not measured large-$x$ (large-$N$) tail. Appropriate methods have been proposed by the above authors, but the resulting values of $S_p$ extracted from the data strongly reflect the precise extrapolation procedure used by the various authors

(Colombi et al. 1996; Munshi et al. 1999).[1] The differences get rapidly very large with increasing order $p$, from factors of 2 for $p = 4$ to already an order of magnitude for $p = 5$. Thus extreme care must be taken in the interpretation of the $S_p$ parameters extracted from the simulations. Rather than introducing sophisticated corrections to extract the large $N$ tail of the counts (with uncontrolled errors due to the badly needed correction for cosmic variance) it may be as accurate (inaccurate) to simply fit a function $h(x)$ to the numerical data and use (8) to get the moments.

## 4    MASS FUNCTIONS

For astrophysical applications, one is usually more interested in the mass functions (the number density of objects defined for instance by a given density threshold) than in the counts-in-cells statistics. Moreover, one may wish to study a wide variety of objects, from low-density Lyman-$\alpha$ clouds (which may even be underdense!) to clusters and massive very dense galaxies (see, e.g., Valageas & Schaeffer 1999 and Valageas et al. 1999 for a detailed description of Lyman-$\alpha$ clouds and galaxies in this framework). Of course, these very different objects are defined by specific constraints, so that they cannot be described solely by the mass function of 'just-collapsed' haloes with the traditional overdensity $\Delta = 177$.

We have determined numerically the multiplicity of various kinds of idealized objects and compared them to theoretical predictions. For this purpose, we use two different methods. The first is the 'spherical overdensity' algorithm (Lacey & Cole 1994), which ranks particles in order of decreasing density and counts haloes defined by the density contrast $\Delta$ by looking down this list (this introduces some double counting, since part of a halo may be counted again at a lower rank: to avoid this, when a new halo is recognized, its particles are removed from the list). The second method is based on a friend-of-friend algorithm with a linking length $b$, which we relate to $\Delta$ through

$$(1 + \Delta) = 178 \left(\frac{0.2}{b}\right)^3. \tag{22}$$

---

[1] To increase the available range, Colombi et al. (1996) correct for the oscillations (typically a factor of 3 from the mean, sometimes an order of magnitude) due to this 'cosmic variance' by means of an an educated guess, fitting a smooth curve of pre-determined shape to the data. To estimate the uncertainty, these authors determine by human judgement what can be considered as a reasonable fit and what cannot. This generates error bars given in the form of a factor $f_Q^{\pm 1}$ (i.e., $S_p$ is within the range $S_{p,\text{mean}}/f_Q$ to $S_{p,\text{mean}} \times f_Q$) with typically $f_Q = 1.1, 1.35$ and 1.65 for $p = 3, 4$ and 5 respectively, whereas the deviations from scaling show, under the same conditions, a scale-dependence by a factor $f = 1.2, 1.5$ and 1.85 respectively. Their interpretation is that, since $f$ is typically larger than $f_Q$ by 10 per cent, this 'proves a small but significant departure from the stable clustering predictions' in the form of a scale-dependence of the coefficients $S_p$. Whereas we think that such a procedure (see Colombi, Bouchet & Schaeffer 1994) to extract information on the large $N$ behaviour, though somewhat indirect, is reasonable in the absence of any better way, it is not free from systematic biases and the associated correction may not be achieved at the accuracy needed to back the claim of the former authors. Indeed, a subsequent work (Munshi et al. 1999), using a different computation, shows that the numerical data for large $x$ are at least consistent with the assumption of no scale-dependence at all of the coefficients $S_p$.

### 4.1 The Press–Schechter approximation for just-collapsed haloes

Most studies have focused on the mass function of 'just-collapsed' (or 'just-virialized') haloes which are defined by a density contrast in the actual non-linear density field $\Delta \simeq 177$ (for $\Omega = 1$). Indeed, this is the quantity which is considered by the popular Press–Schechter (PS) prescription (Press & Schechter 1974). The idea of this formulation is to recognize in the early universe, when density fluctuations are still Gaussian and described by the linear theory, which overdensities will eventually collapse and form virialized objects. Thus one associates to any linear density contrast $\delta_L$ obtained by the linear theory ($\delta_L \propto a$ for a given fluctuation of fixed mass) a non-linear density contrast $\Delta$ provided by the spherical model. Next, one assumes in addition that collapsed objects virialize at a radius equal for instance to one-half their turn-around radius at the time when the spherical dynamics predicts a singularity. Then one obtains that when $\delta_L$ reaches the threshold $\delta_c \simeq 1.69$, a virialized halo with a density contrast $\Delta \simeq 177$ has formed. Finally, one identifies the mass fraction $F_\Delta(> M)$ within such objects of mass larger than $M$ with the fraction of matter which is above the threshold $\delta_c$ at scale $M$ in the linear universe:

$$F_\Delta(> M) = F_L(> \delta_c; M) = \int_{\delta_c}^{\infty} \frac{\mathrm{d}\delta}{\sqrt{2\pi}\sigma(M)} \mathrm{e}^{-\delta^2/(2\sigma^2)}. \qquad (23)$$

Then the mass-derivative of the previous quantity provides the mass function of virialized haloes:

$$\mu(M) \frac{\mathrm{d}M}{M} = -2 \frac{\mathrm{d}F_\Delta}{\mathrm{d}M} \mathrm{d}M = \sqrt{\frac{2}{\pi}} \nu \mathrm{e}^{-\nu^2/2} \frac{\mathrm{d}\nu}{\nu} \qquad (24)$$

with

$$\nu = \frac{\delta_c}{\sigma(M)}. \qquad (25)$$

Here we defined $\mu(M) \,\mathrm{d}M/M$ as the fraction of matter which is enclosed in objects of mass $M$ to $M + \mathrm{d}M$. Note that in (24) we have arbitrarily multiplied the mass function by the usual factor of 2 so as to get the proper normalization to unity. We must, however, emphasize that this normalization correction is not justified in the present case. Indeed, although this multiplicative factor of 2 was recovered rigorously by Bond et al. (1991) using the excursion sets formalism for a top-hat in $k$, taking into account the cloud-in-cloud problem, this result does not apply to more realistic filters like the top-hat in $R$ used here. In fact, as shown in VS (and noticed by Peacock & Heavens 1990 through numerical results), this correction factor goes to unity at large masses. So this factor is not constant (and equal to 2) but $\nu$-dependent. This simple normalization procedure (24), nevertheless, leads to a scaling law in the parameter $\nu$: the mass function $\mu(\nu) \,\mathrm{d}\nu/\nu$ does not depend any longer on the initial power spectrum. We present in Fig. 7 the comparison of our numerical results with the PS prescription. We can check in the figure that the mass functions obtained by both methods are consistent. Note that the numerical points correspond to averages over different output times (weighted by the number of haloes) of the mass functions realized in the simulations. Although there is some scatter, we checked that all curves superpose on the mean mass function shown in Fig. 7. We can note that our results are consistent with the scaling in $\nu$ obtained from the PS approach.

Thus we can see, as was already checked by many authors (e.g.

Efstathiou et al. 1988; Kauffmann & White 1993; Lacey & Cole 1994), that the PS mass function (shown by the dashed line) agrees reasonably well with the numerical results. Indeed, although there are some small but significant discrepancies (especially at the low-mass end, where the slope seems to tend towards the non-linear prediction). This could be expected in view of the simplicity of this approach but the agreement is still rather good for such a simple model. A drawback of the PS approach is that it is clearly limited to the mass function of 'just-collapsed' objects and does not provide by itself predictions for mass functions defined at other density contrasts.

### 4.2 The scaling model for the halo multiplicity

Predictions for the mass function of objects defined by an arbitrary density contrast $\Delta$ in the actual non-linear density field can be obtained within the framework of the scaling model, as shown in detail by VS. These predictions are valid for *any* value of $(1 + \Delta)$, however large or small (even below unity!), provided the conditions (6) are met. As was the case for the counts-in-cells, the mass function exhibits a scaling law in the parameter $x$:

$$\mu(M) \frac{\mathrm{d}M}{M} = x^2 H(x) \frac{\mathrm{d}x}{x}, \qquad (26)$$

where we still have $x = (1 + \Delta)/\bar{\xi}(R)$. Note that here $R$ is the actual size of the halo (as opposed to the 'mass scale' $R_L$, the radius an object of the same mass would have in a uniform density universe, which enters for instance in the PS mass function). The scaling function $H(x)$ should be related to $h(x)$ introduced for the counts-in-cells. Indeed, if one identifies the mass within objects (defined by the density threshold $\Delta$) larger than $R$ [i.e., more massive than $M = (1 + \Delta)\bar{\rho}(4\pi/3)R^3$] with the fraction of matter enclosed in cells of scale $R$ with a density contrast larger than $\Delta$, one obtains a simple estimate $H_{\mathrm{cell}}$ of $H(x)$, which reads

$$H_{\mathrm{cell}}(x) = h(x). \qquad (27)$$

Even if this is probably an oversimplified approach, it has been steadily argued (Balian & Schaeffer 1989a; Bernardeau & Schaeffer 1991; VS) at an increasing level of sophistication that the functions $H(x)$ and $h(x)$ can be expected to be close, and that for practical purposes $h(x)$ can be used as a good approximation to $H(x)$. Also, as can be seen in VS, this procedure is found to be very close to the global derivative used in the PS prescription (24). In the scaling model, however, it is applied to the actual non-linear density field rather than to the original Gaussian field, and thus is correctly normalized.

On the other hand, if one defines directly objects of scale $R$ to $R + \mathrm{d}R$ by the constraints that the density contrast is larger than $\Delta$ on scale $R$ but smaller than $\Delta$ on scale $R + \mathrm{d}R$ (thus one tries to recognize *individually* each halo in order to handle the cloud-in-cloud problem), one gets a new scaling function $H_{\geqslant}(x)$, which can be shown (VS) to satisfy (for constant $\Delta$):

$$\begin{cases} \forall x : \quad H_{\geqslant}(x) \leq \dfrac{3}{\gamma} h(x) \\[2mm] x \gg x_s : \quad h(x) \leq H_{\geqslant}(x) \leq \dfrac{3}{\gamma} h(x) \end{cases} \qquad (28)$$

with generically (unless the leading order in the expansion accidentally vanishes) the same asymptotic behaviour at small $x$:

$$x \ll 1 : \quad H_{\geqslant}(x) \propto h(x) \propto x^{\omega-2}. \qquad (29)$$

Moreover, for a tree-model where the many-body correlation functions can be expressed as products of the two-point correlation function, one obtains $H_{\geqslant}(x) = h(x)$ for $x \gg x_s$. Note that for a Gaussian random field the same procedure (that is, to
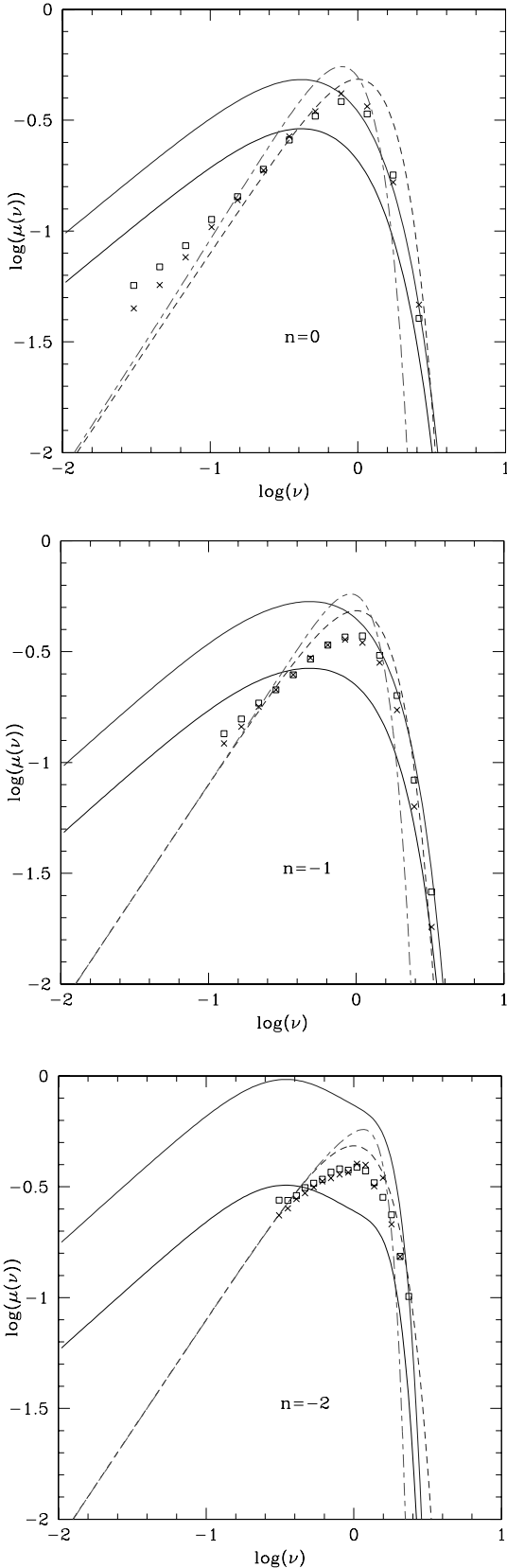
define the mass function by requiring a given overdensity in the linear regime at a given scale $R$ and a lower one at a slightly larger scale, in order to recognize individually each object) would lead to a mass function which diverges at small masses (see VS), and hence divergent total mass due to the severe overcounting. Even for a fixed density contrast $\Delta$, the same mass is counted many times at smaller and smaller scales because of numerous density inversions. Since the fraction of matter (compared to unity) enclosed in objects defined by a density threshold is a direct measure of the severity of the 'cloud-in-cloud' problem, this shows that the latter is indeed severe for Gaussian fluctuations. On the other hand, in the non-linear case when one directly counts the overdensities in the non-linear density field, the normalization is necessarily lower than $3/\gamma$ for the case described above from (28) and can be expected to be close to unity. This shows, as argued by VS, that in the non-linear regime, the overdensities being well-defined, there is no longer any serious cloud-in-cloud problem. The latter still manifests in the sense that the use of $H_{\geqslant}$ induces some slight overcounting, typically of the order of 20 per cent (see VS). This is the same overcounting as the one found in computations for the spherical density algorithm (which has been removed in this case by attributing all the mass to the larger object), and indeed of similar magnitude, as we checked in the numerical simulations. The true constraint, rather than the one on the edge of the haloes used to define $H_{\geqslant}$, which avoids this overcounting, is the condition that the density contrast is smaller than $\Delta$ for *all* scales larger than $R + dR$. This would completely solve the cloud-in-cloud problem. However, the previous formulation leading to $H_{\geqslant}(x)$ should already provide a satisfactory tool. Moreover, it is close to the algorithm actually used in numerical simulations.

The solid curves in Fig. 7 represent the functions $h(x)$ and $3/\gamma$ $h(x)$. From the results described above, we expect the mass function obtained from the numerical simulations to lie below the upper curve for all $\nu$ and between these two curves for large $\nu$ (which corresponds to large $x$) beyond the exponential cut-off. We can see that this is indeed approximately the case for all power spectra. However, it appears that the numerical mass function is significantly different from $h(x)$, especially at the low-mass end. This could be expected, since it does not seem possible to derive a lower bound for $H(x)$ in this domain in the general case. Nevertheless, the slopes of both scaling functions appear to be the same $H(x) \propto h(x)$ for $x \ll x_s$. Note that for large $\nu$ and $x$ ($x > \Delta/10$) the mass function should not behave as in (26), since this domain corresponds to large scales which are no longer in the non-linear regime, so the correlations functions do not obey the scaling (2). The dot-dashed lines correspond to the 'PSs' mass

**Figure 7.** The mass function of 'just-collapsed' haloes defined by the density threshold $\Delta = 177$, displayed in terms of the variable $\nu$. The crosses show the results of a 'spherical overdensity' algorithm, while the squares correspond to a 'friends-of-friends' procedure. The numerical results are averages over different output times from the simulation. The short-dashed curve is the standard PS prescription (note that it does not depend on $n$). The dot-dashed line corresponds to (21), referred to as PSs in the text, which is the same as the PS result in the case that the stable clustering regime is reached (and it can be seen that this is not fully the case here). The lower solid line is the scaling function $h(x)$ obtained from counts-in-cells, while the upper solid line is $3/\gamma$ $h(x)$. The scaling model predicts that in the stable clustering regime the counts are in-between these two curves at large $\nu$, and below the upper one but with generically the same slope at small $\nu$.

function (26) given by the scaling approach with $H(x)$ taken equal to the 'spherical model' scaling function (21). Of course, at small scales it superposes on to the standard PS mass function, as explained in Section 3.3, since in this regime it is equivalent to the
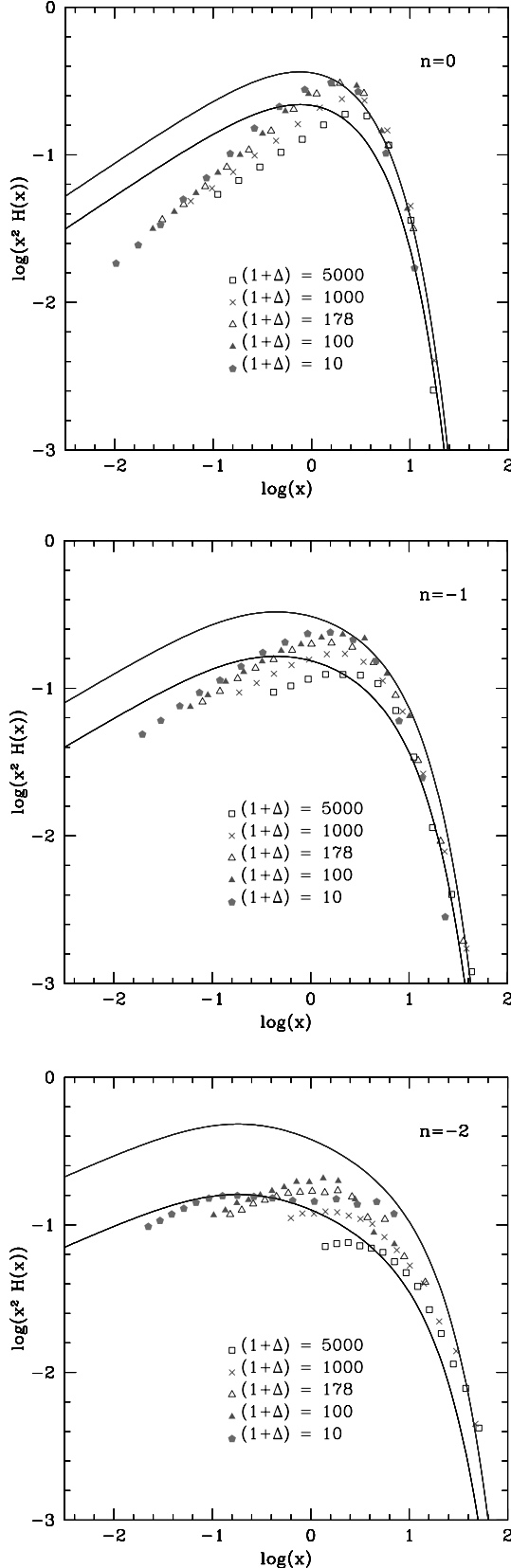
PS prediction. At large scales it differs from the latter, because one leaves the highly non-linear, stable-clustering regime, and the two-point correlation function is no longer given by the asymptotic behaviour $\bar{\xi}(R) = [10/(3\alpha)\sigma(R_\mathrm{L})]^3$; see (12). Note that the PS approach works somewhat better for the mass function than it did for the counts-in-cells statistics, and that, for the contrast $\Delta = 177$ relevant to the present calculations, at large masses the difference with respect to the stable clustering PSs result helps somewhat. What helps also to bring the PS result into agreement with the numerical data is the factor of 2 by which this mass function has been multiplied, as is traditional, despite the fact that numerical calculations (Peacock & Heavens 1990), as well as theoretical considerations (VS), show that this factor should be close to unity at large $x$ (and is expected to be larger at small $x$).

As compared to the standard PS approach, the interest of the formulation (26) for the mass function of 'just-virialized' objects is that it makes a connection with another characteristics of the density field: the counts-in-cells statistics described earlier.

### 4.3 Different constant-density contrasts

The main advantage of the scaling model is that it can deal with more general mass functions. We shall first consider the case of mass functions which are still defined by a constant density contrast, but where $\Delta$ can now take any value. In the scaling approach which led to (26) the quantity $(1 + \Delta)$ is only used to define objects, but no specific value is singled out, as opposed to the PS mass function which explicitly deals with 'just-collapsed' objects (so that it makes sense for only one class of haloes characterized by a non-linear density contrast $\Delta \sim 177$). Hence the relation (26) should hold for any value of $(1 + \Delta)$, in the domain where the scaling (5) holds.

#### 4.3.1 Spherical overdensity agorithm

We show in Fig. 8 the mass functions we obtain from the numerical simulation for various values of the density contrast for the 'spherical overdensity' algorithm. We display the quantity $\mu(M)\,\mathrm{d}\ln M/\mathrm{d}\ln x$ as a function of $x = (1 + \Delta)/\bar{\bar{\xi}}(R)$ [as explained previously, $\bar{\xi}(R)$ was obtained from the same simulation through counts-in-cells; see Fig. 3]. If the scaling (26) holds, all curves should superpose (in the relevant range of validity of the scaling laws) on to the function $x^2\,H(x)$ (we show only the range $x < (1 + \Delta)$, which corresponds to $\bar{\xi} > 1$, but the range of validity could be smaller than this: $\bar{\xi} \gg 1$). The points correspond again to an average over different output times.

We can see that the available counts are pushed much further towards the larger values of $x$ as compared to Fig. 4. This is because we check the neighbourhood of particles to get the haloes, and thus we are guaranteed to be in a region where there really is some mass. To get the statistics of the counts-in-cells, on the other hand, requires us to check randomly over the whole volume, so that the statistics of the less dense but more extended regions are relatively favoured. As will be discussed in more detail in Section



**Figure 8.** The mass functions of haloes defined by various density thresholds $\Delta$ obtained from a 'spherical overdensity' algorithm. Different symbols correspond to different values of $(1 + \Delta)$. The lower solid curve is the scaling function $h(x)$ measured from counts-in-cells, while the upper solid curve is $3/\gamma\,h(x)$. The non-linear model predicts that the counts are in-between these two curves at large $x$, and below the upper one but generically with the same slope for small $x$.

4.4, this amounts in some sense to measuring $xH(x)$ rather than $H(x)$, with better statistics at the large values of $x$ [note, however, that whereas $x^2H(x)$ has a maximum, both the above functions are decreasing for increasing $x$, still favouring the small values of $x$ as
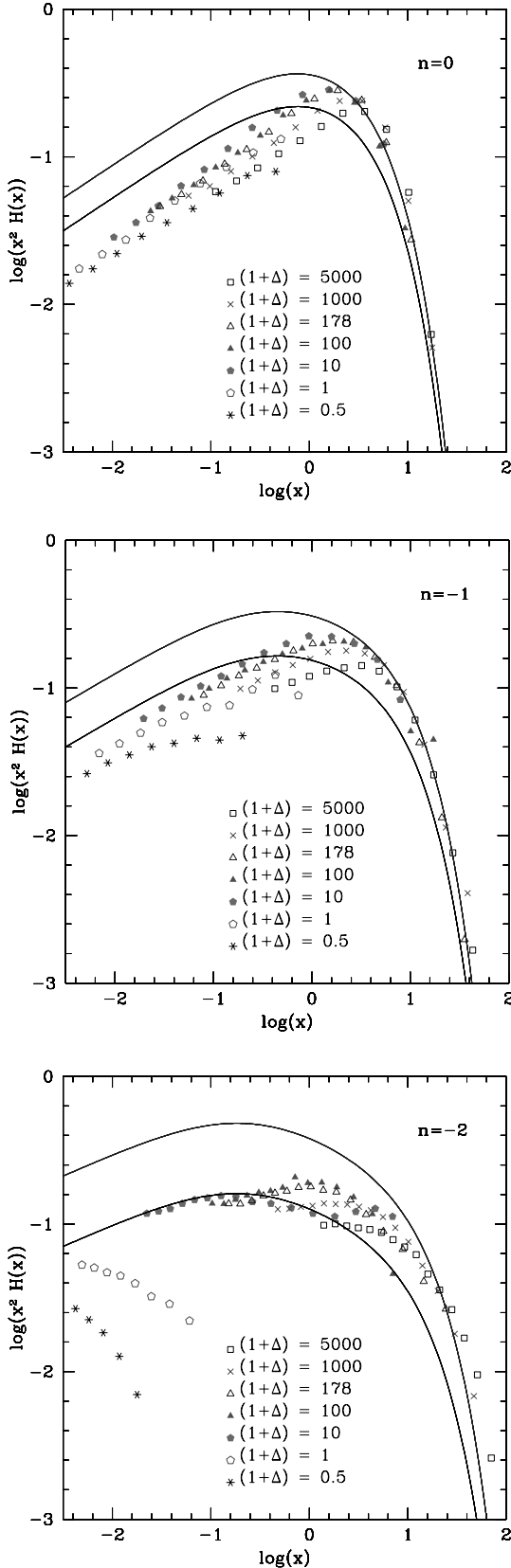


compared to the large ones]. A similar effect was described in Section 3.2 for the measure of $\tilde{\xi}$ as opposed to $\bar{\xi}$.

As expected, all curves lie between $h(x)$ and $3/\gamma\ h(x)$ beyond the exponential cut-off, and are located below $3/\gamma\ h(x)$ for all values of $x$. Moreover, the slope at small $x$ is in most cases close to that for $h(x)$, although for $n = 0$, where the statistics are the best, a distinct difference is apparent: whereas $h(x)$ has a slope (Table 2) $\omega = 0.45$, here the slope is rather $\omega = 0.6$.

Moreover, although all curves superpose beyond the cut-off as predicted, there appears to be a shift in the power-law domain with $(1 + \Delta)$: larger density contrasts lead to a smaller amplitude in this part of the mass function. This drift appears at $x \lesssim 3$ for $(1 + \Delta) = 5000$ and $x \lesssim 1$ for $(1 + \Delta) = 1000$, and has disappeared for $(1 + \Delta) = 178$ [indeed, the curves obtained for $10 \leq (1 + \Delta) \leq 178$ superpose very well].

These deviations will be discussed in the following section.

### 4.3.2 Friend-of-friend algorithm

We show in Fig. 9 the mass functions we obtain from the 'friend-of-friend' algorithm. We can check that they are consistent with the results from the 'spherical overdensity' algorithm. For large $\Delta$ we find as previously that the curves superpose beyond the exponential cut-off, but that there is a drift in the power-law domain.

The advantage of the 'friends-of-friends' algorithm is that we can also consider negative density contrasts, providing a much larger range for the possible variations of $\Delta$. In such a case we count one large halo which extends over the whole box (the clusters linked by the filaments create a percolating network), and also *small underdense objects which appear as density peaks within voids* and are separated from the main cluster by their very low-density surroundings. Thus the mass function defined in this way makes sense only for very small masses (small parameter $x$). Despite the low density, this is still in the strongly non-linear regime, since $x \ll (1 + \Delta)$ so that $\bar{\xi} \gg 1$.

For $n = 0$, we can see that all curves fall on top of each other, down to $(1 + \Delta) = 0.5$ which is rather low at $\log x \lesssim -0.5$. Similarly, for $n = -1$, the results exhibit the scaling theoretically implied by the stable clustering, except for $(1 + \Delta) = 0.5$ at the larger values of $x$ ($\log x \gtrsim -1.5$). For $n = -2$, also, the curves with $(1 + \Delta) = 0.5$ and $(1 + \Delta) = 1$ do not fall on the scaling curve built by the result at larger density contrasts. As shown in Fig. 10, the deviations found for the lower values are seen to be closely associated to the degradation of the statistics (the counts are low at the larger $x$), which occurs for all three values of $n$ we have studied precisely at the same values of $(1 + \Delta)$ and $\log x$ where the deviations are noticed. Moreover, the deviation at large $x$ of the mass functions measured for low density contrasts ($\Delta \leq 0$) from the scaling predictions corresponds to the fact that they make sense only for small $x$, since we must have $x \ll (1 + \Delta)$ so as to

**Figure 9.** The mass functions of haloes defined by various density thresholds $\Delta$ obtained from a 'friend-of-friend' algorithm. Different symbols correspond to different values of $(1 + \Delta)$. The data shown correspond to averages over several simulations. The lower solid curve is the scaling function $h(x)$ measured from counts-in-cells, while the upper solid curve is $3/\gamma\ h(x)$. The non-linear model predicts that the counts are in-between these two curves at large $x$, and below the upper one but generically with the same slope for small $x$.

avoid entering the linear regime where there are no dense spots within underdense regions like the ones we look for here.

So the non-linear scaling prediction is seen to hold down to values of $(1 + \Delta)$ that are unity or even smaller. This is nearly
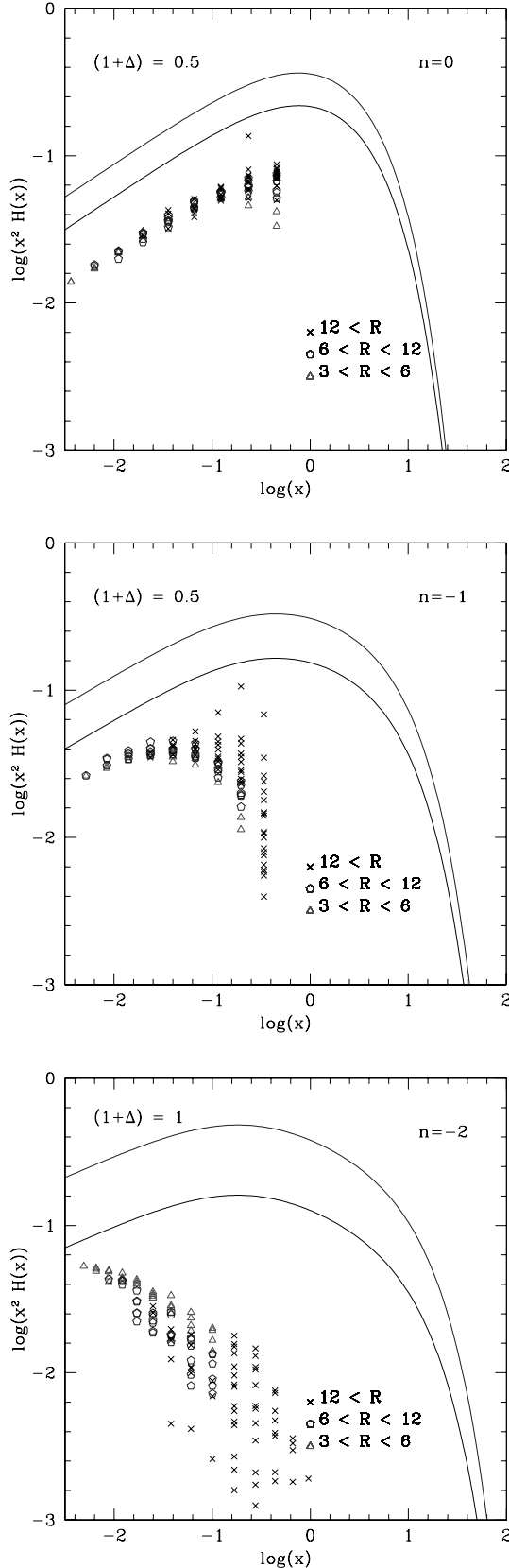


three orders of magnitude below the standard density contrast of 178 usually studied. It has also been tested down to $\log(x) = -2.5$, a real improvement as compared to existing work: values below $\log(x) = -1$ had never been considered previously.

Note that the slopes at small $x$ of the mass function are close to the ones predicted by the theory. In the $n = 0$ case, for instance, $\omega \sim 0.5$, quite close to the slope $\omega = 0.45$ of $h(x)$. The offset seen in Fig. 8 with the 'spherical overdensity' algorithm does not exist in this case. It should be noted that the $n = 0$ case with $(1 + \Delta) = 0.5$ clearly shows (Fig. 9) that the non-linear power-law prediction (and, perhaps more important, the prediction of existence !) for objects that are much denser than their close environment is well verified even in this quite extreme case of very low density, definitely below the average.

Towards the higher densities, we have run calculations up to $(1 + \Delta) = 5000$, a factor of 30 above the usual densities. As for the spherical density algorithm, scaling is well verified. Similarly, at the smaller values of $x$, steadily increasing deviations appear when $\Delta$ is increased, though to a lesser extent. For $n = -1$ and $\log(x) = 0$, the curve for $(1 + \Delta) = 5000$ is below the one for $(1 + \Delta) = 1000$ (that at fixed $x$ corresponds to correlation functions 5 times smaller, and hence to scales $5^{1/1.5} = 2.9$ times larger at fixed time) by a factor of 1.35 and below the $(1 + \Delta) = 178$ curve by a factor of 1.7. The relevant scales are the smallest reachable in the simulation, typically $R = 0.5\,\text{Mpc}$ at $\log(x) = 0$ and $R < 0.3\,\text{Mpc}$ at $\log(x) = -0.4$, for $(1 + \Delta) = 5000$. This is to be compared with the force softening parameter which is $0.2\,\text{Mpc}$ in all the calculations presented here. We have checked the sensitivity of the calculations to variations of this softening parameter. Decreasing the latter by a factor of 2, so as to increase the effect of collisions, lowers the counts by a factor of 1.25 at the scales considered above (a change quite comparable to the deviations from scaling that were found), but has no effect at the larger values of $x$ (the larger scales). For the calculation of the correlation function, at $\bar\xi > 1000$, similarly, deviations of the computation appeared at small scales. So there is a limit towards the large densities and the smaller values of $x$ beyond which the numerical tests are no longer conclusive, since binary collisions due to the discreteness of the points in the simulation start to play a non-negligible role.

Although the previous discussion leads us to attribute the lack of objects below some value of $x$, for a given (large) density contrast, to the fact that the smallest available scale in the simulation has been reached, this is an important point to be discussed. Note that the theoretical prediction (see VS) for $H(x)$ extends to all values of $x$ (including the lower ones for which there are no numerical data), and that, whatever the density contrast, the area under the scaling curve is unity [it is actually slightly above for $H_{\geqslant}(x)$, but is unity if corrections to avoid double counting are made]. This means that however large the required density threshold is, it defines a way to distribute all the mass among objects having this density contrast. The theoretical prediction thus calls for very strong *subclustering* at all density levels. On the other hand, the simulations do not provide enough power at small

**Figure 10.** The mass functions obtained from a 'friend-of-friend' algorithm for $(1 + \Delta) = 0.5$ (with $n = 0$ and $-1$) and $(1 + \Delta) = 1$ (with $n = -2$), as in Fig. 9. Different symbols correspond to different ranges for the comoving size $R$ of the haloes. The various points located at the same value of $x$ for a given range of $R$ correspond to different times (and slightly different $R$ within the allowed range). They should superpose due to the self-similarity induced by the power-law initial conditions.

*x* for large overdensities: there is barely more than 50 per cent of the mass in objects of contrast 5000, for instance, showing an increasing lack of high-density objects. Again, this apparent difference is worth investigating thoroughly in future, more
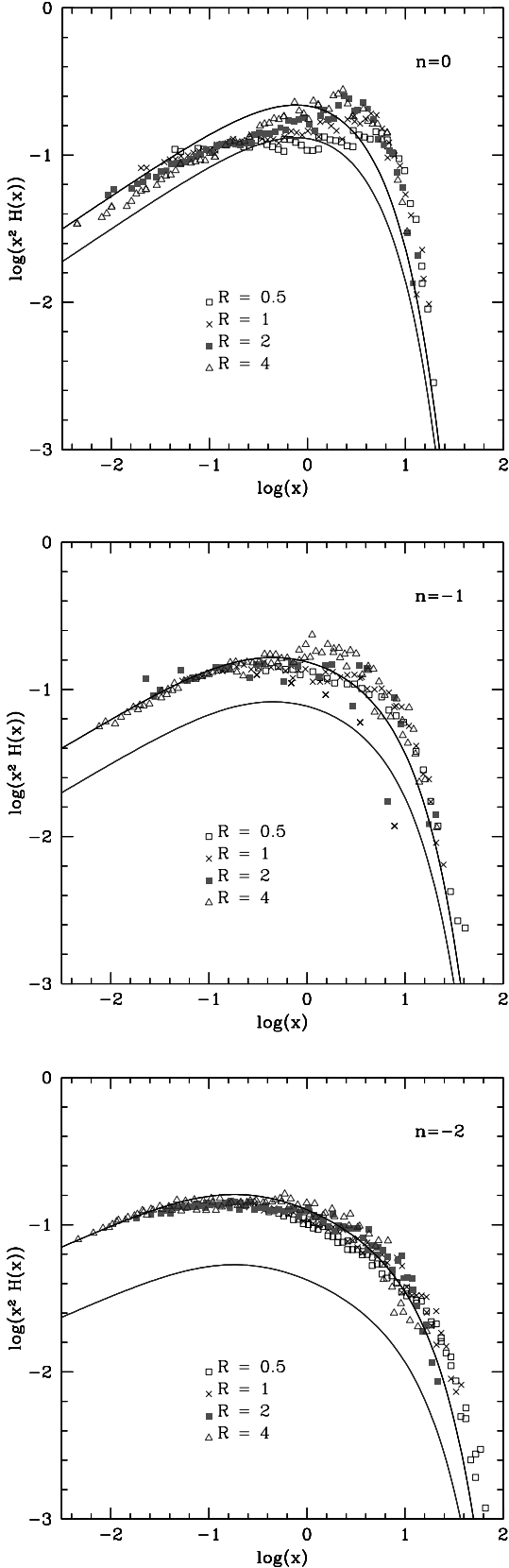


extended simulations, to see whether subclustering up to extremely high overdensities is present down to very small scales or not. However, as shown in Valageas (1999), note that the reasonable agreement of the numerical results with our scaling model already shows that there is a large amount of subclustering. It has been steadily argued (Balian & Schaeffer 1989a,b) that the existence and the behaviour of these substructures are the base of the scaling model and govern the properties of the density field.

We have tested the scaling model for the multiplicity function for vastly different density contrasts, spanning four orders of magnitude, from $(1 + \Delta) = 0.5$ to $(1 + \Delta) = 5000$, finding non-linear objects at every density. We have shown that up to the small-scale limit where collision effects begin to play a role, and to the low-density limit where deviations from self-similarity start to appear, the scaling model provides a reasonable approximation to the mass functions obtained in the simulations. Also, we can note that the scaling model gives surprisingly good results in domains which are beyond its expected range of validity. For instance, the curves for $(1 + \Delta) = 10$ and $(1 + \Delta) = 178$ agree in the numerical results down to $\bar{\xi} \sim 1$. Hence, although the model may not be perfect, it is still quite powerful as it allows one to get a good estimate of the mass functions of very different objects. Moreover, it clarifies an interesting link with another statistical analysis of the density field, namely the counts-in-cells.

### 4.4 Constant radius

In practice, one may also be interested in objects which are no longer defined by a constant density threshold but by a condition of the form $(1 + \Delta) \propto R^{-\beta}$. The predictions of the scaling model for such a case were studied in VS. It happens that for astro-physical objects like galaxies or Lyman-$\alpha$ clouds the constraints which define these mass condensations can be approximated in some range by the requirement that their radius is constant and equal to a given scale which may be associated in the first case to a cooling radius and in the second to a Jeans length (see Valageas & Schaeffer 1999 and Valageas et al. 1999 for more details). This corresponds to the limit $\beta \rightarrow \infty$. Then one has to add the supplementary constraint that the density profile is locally decreasing (since one usually wants to consider peaks and not valleys). In this specific case, one obtains the relations (see VS):

$$H_{\text{cell}}(x) = h(x) \tag{30}$$

for the simple model. More realistically, one can define (see VS) a scaling function $H_{\geqq}(x)$ for the mass distribution of objects of fixed radius and make the statistics of the overdensity $(1 + \Delta)$ [and hence of the mass, since we have $M \propto (1 + \Delta)$] by requiring such a halo to have a density contrast larger than $\Delta$ at scale $R$ and smaller than $\Delta$ at a slightly larger scale. Thus one considers individually each object, defined by the fixed radius $R$ and its density contrast $\Delta$ (which gives its mass), making sure that it is

---

**Figure 11.** The mass functions of haloes defined by various comoving radii $R$, obtained from a 'modified spherical overdensity' algorithm (see main text). Different symbols correspond to different values of $R$. Note that for each radius we display the results obtained at several times which correspond to various values of $\bar{\xi}$. The upper solid curve is the scaling function $h(x)$ measured from counts-in-cells, while the lower solid curve is $\gamma/3 \, h(x)$. The non-linear model predicts that the counts are in-between these two curves at large $x$, and below the upper one but generically with the same slope for small $x$.

surrounded by regions of lower density. Then one obtains the bounds

$$
\begin{cases}
\forall x : & H_{\geqslant}(x) \leq h(x) \\
x \gg x_{\mathrm{s}} : & H_{\geqslant}(x) \geq \gamma/3\, h(x).
\end{cases}
\tag{31}
$$

Obviously this procedure is quite similar to the counts-in-cells, so we can expect the scaling function $H(x)$ to be very close to $h(x)$.

We show in Fig. 11 the mass functions obtained in this way from the numerical simulations. We simply use a modified version of the 'spherical overdensity algorithm', looking at particles in order of decreasing density and defining haloes as objects of constant size $R$ around density peaks. The scaling with the variable $x$ is well verified, for all values of the spectral index $n$, with a result that is very close to the prediction (30). There seem, nevertheless, to be more counts at large $x$ (large masses): the first of the bounds (31) of the 'improved' estimate $H_{\geqslant}(x)$ (in the sense it is closer to the spherical overdensity procedure) seems to be somewhat violated. Note, however, that the curves obtained for different radii (and times) superpose fairly well, which shows that the predicted scaling in $x$ is verified (within the numerical scatter). In fact, this small deviation is probably due to the definition of $H_{\geqslant}(x)$ itself and not to a failure of the scaling laws (2). Indeed, this estimate of the mass function is derived from specific counts-in-cells (with the characteristic that these cells consist of an internal sphere surrounded by a small corona), so that one can miss the most massive high-density haloes by looking at a sphere which is not exactly centred on to the underlying halo. This decreases the mass enclosed in this sphere, which is maximum for a cell correctly centred. On the other hand, in the simulation one directly draws the spheres from the highest density peaks, so that one always counts the largest amount of matter which can be attached to a given halo (if the object is approximately spherically symmetric). This latter procedure (looking at the peaks) is not included in $H_{\geqslant}(x)$ and, because of this small 'mis-placement' of the spheres, it slightly underestimates the number of very high-density and massive haloes. We note that a similar, but very small, deviation may be seen for the mass functions shown in Figs 8 and 9, for the same reason. We also note that the mass function shown in Fig. 11 allows one to probe deeper into the exponential cut-off of $H(x)$, and hence of $h(x)$, as compared to the counts-in-cells shown in Fig. 4. This could also be expected from the fact that in this procedure 'cells' are drawn directly around highest density peaks, which are thus well accounted for, while for the statistics of $P(N)$ the density peaks can be divided between several cells.

## 5  CONCLUSIONS

In this paper we have presented a comparison of the results obtained from numerical simulations to the analytical predictions implied by the Press–Schechter (Press & Schechter 1974) prescription and the scaling model (Balian & Schaeffer 1989a; VS).

We have first checked that the two-point correlation functions follow the behaviour predicted by the stable-clustering Ansatz, as shown by other studies. However, although there is a qualitative agreement between various works, the exact value of the amplitude of the two-point correlation function in the highly non-linear regime still remains poorly determined, as there remains some discrepancy between different studies. Next, we have shown that the scaling model provides a good description of the counts-in-cells statistics. The characteristic scaling functions

$h(x)$ we obtain over the unprecedented range $-2.5 < \log x < 1$ agree reasonably well with previous estimates. Nevertheless, the asymptotic behaviour of the exponential cut-off is not very well constrained for $n = -2$ due to the limited range of scales available in the simulations.

Then we considered the mass function of 'just-collapsed' objects, which is the quantity most authors have focused on. As was already noticed by many studies, we find that the PS approximation works reasonably well for density contrasts of $\simeq 200$ (although there are some discrepancies). On the other hand, the numerical results are also consistent with the predictions of the scaling model (although they do not provide the exact value of the mass function). Next, we have studied more general mass functions defined by various density contrasts that vary by four orders of magnitude (including negative density thresholds!). The scaling model (which is the only currently available analytical tool to handle these quantities) was shown to provide a reasonable estimate of these mass functions.

Finally, we considered the limiting case of objects defined by a constant radius constraint (which arises in an astrophysical context from cooling conditions). We have shown that the scaling model also works very well for such mass functions. Some small deviations appear in certain regimes. We make specific suggestions on which biases may appear in the simulations, and show they are of the right order of magnitude. Although these biases probably explain the observed scatter, it is quite clear that we cannot check the scaling prediction better than this scatter. It remains to be verified in more powerful simulations whether (at least part of) these deviations can be attributed to some violation of the scaling predicted by theory, or if these deviations indeed disappear and thus simply reflect the fact that we have pushed the present simulation as far as possible, and reached its limits.

Thus the scaling model provides a reasonable description of the density field in the non-linear regime (although there are some deviations in certain regimes, they remain reasonably small for practical purposes). Moreover, it allows one to link two different properties of the latter: the counts-in-cells statistics and the mass functions. In addition, it can be used to obtain many different mass functions (in addition to the usual 'just-collapsed' haloes), which is of great interest for practical purposes when one intends to model various objects like Lyman-$\alpha$ clouds or galaxies which clearly cannot be defined by the sole constraint $\Delta = 177$. Obviously, our study should be extended to more realistic power spectra which are no longer power-laws (e.g., CDM) and to different cosmologies (low-density universes).

## REFERENCES

Balian R., Schaeffer R., 1989a, A&A, 220, 1
Balian R., Schaeffer R., 1989b, A&A, 226, 373
Bernardeau F., 1996, in Ansari R., Giraud-Heraud Y., Tran Thanh Van J., eds, Proc. XXXIth Moriond meeting, Editions Frontières, Gif-sur-Yvette, p. 187
Bernardeau F., Schaeffer R., 1991, A&A, 250, 23
Bond J. R., Cole S., Efstathiou G., Kaiser N., 1991, ApJ, 379, 440
Bouchet F. R., Schaeffer R., Davis M., 1991, ApJ, 383, 19
Colombi S., Bouchet F. R., Schaeffer R., 1994, A&A, 281, 301
Colombi S., Bouchet F. R., Schaeffer R., 1995, ApJS, 96, 104
Colombi S., Bouchet F. R., Hernquist L., 1996, ApJ, 465, 14
Colombi S., Bernardeau F., Bouchet F. R., Hernquist L., 1997, MNRAS, 287, 241

Couchman H. M. P., 1991, ApJ, 368, 23

Davis M., Peebles P. J. E., 1977, ApJS, 34, 425

Davis M., Efstathiou G., Frenk C., White S. D. M., 1985, ApJ, 292, 371

Efstathiou G., Frenk C. S., White S. D. M., Davis M., 1988, MNRAS, 235, 715

Hamilton A. J. S., Kumar P., Lu E., Matthews A., 1991, ApJ, 374, L1

Jain B., Mo H. J., White S. D. M., 1995, MNRAS, 276, L25

Kauffmann G., White S. D. M., 1993, MNRAS, 261, 921

Lacey C., Cole S., 1994, MNRAS, 271, 676

Munshi D., Bernardeau F., Melott A. L., Schaeffer R., 1999, MNRAS, 303, 433

Padmanabhan T., 1996, MNRAS, 278, L29

Padmanabhan T., Cen R., Ostriker J. P., Summers F. J., 1996, ApJ, 466, 604

Peacock J. A., Heavens A. F., 1990, MNRAS, 243, 133

Peebles P. J. E., 1980, The Large Scale Structure of the Universe. Princeton Univ. Press, Princeton

Peebles P. J. E., 1982, ApJ, 263, L1

Press W., Schechter P., 1974, ApJ, 187, 425

Valageas P., 1999, A&A, 347, 757

Valageas P., Schaeffer R., 1997, A&A, 328, 435 (VS)

Valageas P., Schaeffer R., 1999, A&A, 345, 329

Valageas P., Silk J., 1999, A&A, 347, 1

Valageas P., Schaeffer R., Silk J., 1999, A&A, 345, 691

This paper has been typeset from a TEX/LATEX file prepared by the author.